Energy Conversion and Management: X 1 (2019) 100004

Contents lists available at ScienceDirect

Energy Conversion and Management: X

journal homepage: www.journals.elsevier.com/energy-conversion-and-management-x

Combined water desalination and electricity generation through a humidification-dehumidification process integrated with photovoltaic-thermal modules: Design, performance analysis and techno-economic assessment

Paolo Gabrielli[a], Matteo Gazzani[b], Nicolò Novati[c], Lara Sutter[a], Riccardo Simonetti[c], Luca Molinaroli[c], Giampaolo Manzolini[c], Marco Mazzotti[a]

[a] Institute of Process Engineering, ETH Zurich, 8092 Zurich, Switzerland
[b] Copernicus Institute of Sustainable Development, Utrecht University, Heidelberglaan 2, 3584 CS Utrecht, The Netherlands
[c] Department of Energy, Politecnico di Milano, Via Lambruschini 4, 20156 Milano, Italy

ARTICLE INFO

Keywords:
Water-energy nexus
Solar desalination
Remote water and energy access
Off-grid generation
HDH
PVT

ABSTRACT

Humidification-dehumidification (HDH) processes have proved to be a promising solution for small-scale desalination, appropriate for water production in off-grid locations where the water demand does not justify the installation of conventional large-scale systems. With this contribution, we investigate the design and operation of an HDH process coupled with photovoltaic-thermal (PVT) solar modules for the simultaneous generation of clean water and electricity. The HDH system consists of established technologies, namely a humidification column and a heat exchanger, and is simulated through a commercial software accounting for heat and mass transfer limitations. On the other hand, PVT modules are a relatively new technology and their performance is determined experimentally to characterize the simultaneous generation of electricity and heat under realistic operating conditions. Based on the maximum-efficiency ratio of water to air mass flow rates, the optimal design of the system is determined for a wide range of ambient conditions by evaluating the impact of saline water flow rate, PVT configuration and HDH size on the amount of clean water produced. Then, the optimal operation of the system is characterized as function of the ambient conditions for a fixed system design. The state of the system is represented by the maximum process temperature, at the outlet of the PVT modules, whereas the performance is evaluated in terms of clean water and electricity generation. Finally, a techno-economic assessment is carried out to compare the proposed technology against conventional solar-driven HDH units, which use thermal and photovoltaic panels, for a wide range of electricity price, ambient conditions, amount of yearly water produced and size of the HDH process.

1. Introduction

Today, about 800 million people lack access to potable water and about 1.2 billion people have no access to electricity [1]. At the same time, the population and economical growth of developing countries is leading to a projected increase in water and energy demands of about 50% and 100% by 2050, respectively [2]. Saline water desalination is a promising technology for water security; globally, 90 million cubic meters of water is desalinated every day, with a total energy consumption above 26 million tonnes of oil equivalent per year. More than 99% of this energy demand is satisfied by fossil fuels, resulting in CO_2 emissions of more than 76 million tonnes per year [3]. This calls for renewable-based, sustainable desalination systems, particularly in remote locations where energy generation and transmission have high economic and environmental impacts [4,5].

Humidification-dehumidification (HDH) systems for desalination have not been deployed yet, due to their low energy efficiency and water productivity with respect to conventional technologies, such as multi-effect distillation (MED) and reverse osmosis (RO) [6]. Despite such disadvantages, HDH systems do not require sophisticated components and expensive maintenance, have proven to provide a promising solution for small-scale desalination, and to be appropriate for water production in off-grid locations where the water demand does not justify the installation of conventional large-scale systems [7,8]. Furthermore, the low water productivity, generally lower than 10%, is a potential benefit in the aforementioned contexts as it leads to low levels of brine concentration, thus avoiding the need of expensive brine disposal. HDH uses a carrier fluid to separate clean water from the saline feed. In its simplest form, the process consists of three sub-systems: carrier/water heater, humidifier (i.e. evaporator), and dehumidifier

https://doi.org/10.1016/j.ecmx.2019.100004

Available online 23 January 2019

Nomenclature

A	area of solar collectors, [m^2]
B	geometrical factor, [m]
C	total capital cost, [€]
c	cost of clean water, [€/m^3]
c_p	heat capacity at constant pressure, [kJ/(kg K)]
D	diameter of heat and mass exchanger, [m]
E	net electricity production, [kW]
e	specific net electricity production, [kWh/kg]
F	heat flux, [kW/m^2]
G	dry air mass flow rate, [kg/s]
H	height of the humidifier, [m]
h	specific enthalpy, [kJ/kg]
h^*	specific enthalpy per unit dry air, [kJ/kg_G]
I	solar irradiance, [W/m_2]
J	mass flux, [kg/(sm^2)]
K	annual cost, [€/yr]
k	specific annual cost, [€/kg]
L	saline water flow rate, [kg/s]
l	saline water flow rate per unit solar area, [kg/(hm^2)]
M	clean water flow rate, [kg/s]
N	number of solar modules, [–]
P	PVT electrical power, [kW]
p	pressure, [bar] electricity price, [€/kWh]
Q	heat consumption, [kW]
q	specific heat consumption, [kWh/kg]
r	humidifier section-to-solar area ratio, [–]
T	temperature, [°C]
U	moist air mass flow rate, [kg/s]
y	mole fraction, [–]
W	yearly water production, [kg/yr]
w	clean water flow rate per unit solar area, [kg/(hm^2)]
z	spatial coordinate (independent variable), [m]

Greek letters

α	PVT empirical coefficient, [W/(m^2K)]
β	PVT pressure drop coefficients, [(bar s^2)/kg^2], [(bar s)/kg]
γ	PVT power coefficient, [%/K]
δ	discount rate, [–]
η	efficiency, [–]
λ	fraction of total cost, [–]
τ	technology lifetime, [y]
Ψ	enthalpy pinch, [kJ/kg_{da}]
Ω	optimal saline water-to-dry air flow rate ratio in dehumidifier, [–]
ω	humidity ratio, [kg_L/kg_G]

Subscripts

*	lower range
amb	ambient
avg	average
cell	solar cell
e	electrical
G	dry air
in	inlet
inv	inverter
inst	installation
L	saline water
M	clean water
m	solar module
maint	maintenance
max	maximum
o	optical
out	outlet
p	parallel-connected solar modules
s	series-connected solar modules
t	thermal
U	moist air

Superscripts

*	upper range, per unit dry air
0	negative cost threshold, reference conditions
deh	dehumidifier
hum	humidifier

Acronyms

BoP	balance of plant
CAOW	closed-air open-water
HDH	humidification-dehumidification
LMTD	logarithmic mean temperature difference
PV	photovoltaic panels
PVT	photovoltaic-thermal panels

(i.e. condenser) [9]. HDH systems are classified based on (i) the type of energy used, (ii) the cycle configuration, and (iii) whether water or carrier is heated up. While several cycle configurations have been investigated, reviewed by Müller-Holst et al. [10] and Narayan et al. [11], the closed-air open-water (CAOW), water-heated configuration has been proven to be the most energy-efficient solution and it is therefore considered in this work (see Fig. 1). A review of the design strategies for conventional and modified CAOW processes is provided by Elmutasim et al. [12]. Furthermore, whereas different carriers have been studied, including hydrogen, helium, CO_2 [13,14], here we consider air as carrier fluid, as this is in line with the considered applications, i.e. simple, small-scale, off-grid desalination units.

Several studies have focused on reducing the energy consumption of the HDH process, being this one of the major issues. First, Müller-Holst showed that entropy generation, and thus energy consumption, is minimized when the stream-to-stream temperature difference is kept constant across the system, and tried to achieve this condition by adjusting the water and air flow rates along humidifier and dehumidifier [15]. Later, Narayan et al. introduced the notion of modified heat capacity rate ratio as the ratio of the maximum difference in enthalpy rates of the cold and hot streams in heat and mass exchangers; they showed that the entropy generation of an HDH process is minimized when such heat capacity rates are equal in the dehumidifier, which translates into an optimal ratio of water to air mass flow rates in the dehumidifier [16–18]. In this case, the system is said to be balanced. We have recently reached the same conclusion through an analysis based on equilibrium theory, which shows how the optimal operating condition is independent of heat and mass transfer limitations [19].

Based on such findings, several studies have presented optimized multi-stage layouts with varying water-to-air mass flow rate ratios [20–34]. Furthermore, many studies have investigated the integration of the HDH cycle with solar modules both computationally [30,35,36] and experimentally [32,37–41], though almost all of them have considered thermal collectors as the energy source. The coupling of cooled photovoltaic (PV) modules with the HDH technology was first investigated by Wang et al., who analyzed the effect of the process temperature and of the convection mode on the amount of clean water produced [42]. Later, Giwa et al. studied the environmental impact of

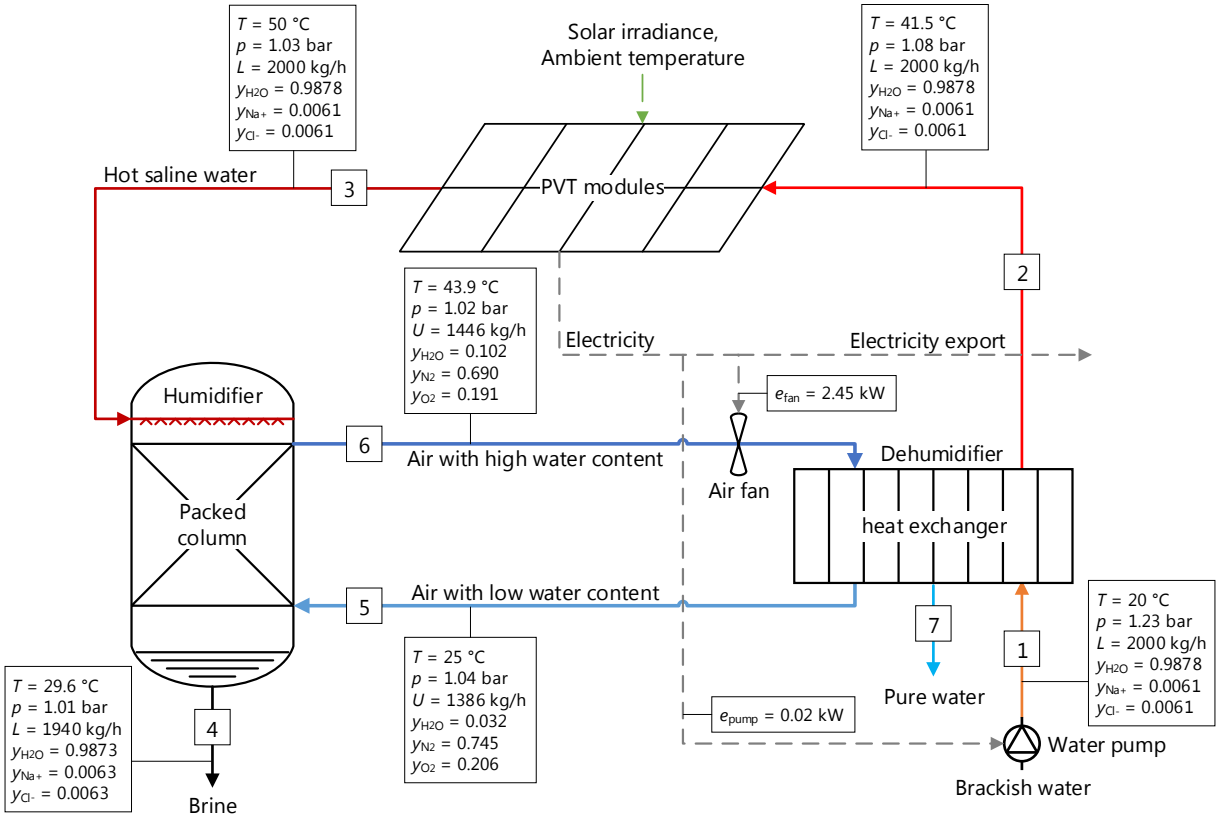

Fig. 1. Schematic of a closed-air, open-water, water-heated HDH system with PVT modules as energy source. The relevant streams are characterized for an exemplary simulation in terms of temperature, T, pressure, p, mass flow rates, L and U for saline water and moist air respectively, and molar fractions, y.

the PV-HDH technology [43], whereas Elsafi evaluated the efficiency of a cogeneration unit consisting of an air-heated HDH cycle and concentrated photovoltaic-thermal (CPVT) collectors and compared the cost of water produced against that obtained with other HDH-based desalination technologies [44]. However, neither the optimal operation of such systems, nor their optimal design for the cogeneration of clean water and electricity, have been investigated yet.

In this study, we consider the HDH system operating at the optimal water-to-air mass flow rate ratio, Ω, mentioned above. Referring to Fig. 1, this is given by

$$\Omega = \frac{\Delta h_{\mathrm{U}}^{\max}}{\Delta h_{\mathrm{L}}^{\max}} = \frac{h_{\mathrm{U}}^{*}(T_6) - h_{\mathrm{U}}^{*}(T_1)}{h_{\mathrm{L}}(T_6) - h_{\mathrm{L}}(T_1)} \tag{1}$$

where T is the temperature, h the specific enthalpy and h^* the specific enthalpy per unit dry air; the subscripts L and U refer to saline water and moist air, respectively. When solar energy is adopted to drive the HDH process, the optimal operating condition given by Eq. (1) depends on the ambient conditions, namely ambient temperature and solar irradiance. We take this into account by determining feasible and optimal operating conditions, in terms of clean water and electricity generation, of an HDH process coupled with photovoltaic-thermal (PVT) solar modules as function of ambient conditions. Furthermore, we study the optimal design of the system to quantify the impact of the PVT configuration and of the HDH size on clean water and electricity production for several ambient conditions. Moreover, the cogeneration of clean water and electricity is investigated by evaluating the total cost of clean water as a function of the electricity price. This cost is compared to that of conventional solar-driven HDH processes, which use thermal and PV panels, for a wide range of ambient conditions, yearly water production, and size of the HDH process.

This paper is structured as follows. Section 2 presents the mathematical models implemented to simulate the different components of the process, namely HDH and PVT. In Section 3 the main results are presented and discussed. Finally, in Section 4 conclusions are drawn.

2. Mathematical model

A scheme of the process, with a single-stage HDH system and PVT solar modules as energy source, is shown in Fig. 1. The relevant streams are characterized for an exemplary simulation in terms of temperature, T, pressure, p, mass flow rates, L and U for saline water (or brine) and moist air, respectively, and composition expressed in mole fractions, y. Cold saturated air is heated-up in the humidifier, where it enters in contact with the hot saline water, thus increasing its vapor pressure. A fraction of the saline water stream evaporates, thus increasing the water content of the air stream. Then, the hot saturated air enters the dehumidifier, where it is cooled down by cold saline water, causing some of the water vapor to condense, thus producing a stream of pure water. The saline water, which is pre-heated in the dehumidifier, is heated up to the maximum temperature in the solar modules and discharged by the humidifier in the form of a concentrated brine.

As inputs the mathematical model has (i) the flow rate and inlet conditions of the saline water, (ii) the ambient conditions, and (iii) the geometry and the performance coefficients of the considered components, i.e. HDH system and PVT modules. Based on these, it determines (i) the flow rate and temperature profiles of water and air, (ii) the thermal and electrical energy consumption, and (iii) the electricity production. All the input parameters assumed within the mathematical model are summarized in Table 1. The inlet saline water is characterized in terms of temperature and salinity, whereas the relevant ambient conditions are ambient temperature and solar irradiance. The time profiles of ambient conditions implemented in this work are discussed in Section 3. We note that while such assumptions are required to perform calculations, they do not affect the generality of the proposed model and the relevance of the results.

Table 1
Parameters of the mathematical model.

Saline water inlet conditions (dehumidifier)	
Temperature	20 °C
Salt mass concentration	20 g/l
Humidifier	
Type	Packed-bed column
Flow	Counter-current (plug flow)
Packing	Flexring (Koch-Glitsch) [45]
Fraction of flooding velocity	80% [46]
Height discretization	0.1 m (see Supplementary Material)
Film discretization rate	1 (see Supplementary Material)
Dehumidifier	
Type	Air-water heat exchanger
Flow	Counter-current
Heat transfer coefficient	50 W/(m^2 K) [47]
Internal discretization	10 zones with LMTD (see Supplementary Material)
Heat losses	5% of total duty (see Supplementary Material)
PVT panels [48]	
Reference electrical power, P^0	153 W/m^2
Reference solar irradiance, I^0	1000 W/m^2
Reference cell temperature, T^0_{cell}	298.15 K
Power temperature coefficient, γ	0.42%/K
Optical efficiency, η_o	0.50 (see Appendix B)
Loss coefficient, α	11.2 W/(m^2 K) (see Appendix B)
Pressure drop coefficient, β_1	36.5 (bar s^2)/kg^2
Pressure drop coefficient, β_2	2.66 (bar s)/kg
Area of PVT/PV module	1.6 m^2
Area of thermal module	2.2 m^2 [49]
Peak electricity production of PVT/PV module	0.25 kW
Auxiliaries	
Isentropic efficiency of water pump and air fan	0.65

In the following, the mathematical models implemented to simulate the HDH system and the PVT modules are presented. The numerical procedure adopted to compute a simulation of the overall process is discussed in Appendix A.

2.1. Humidification-dehumidification system

The HDH system is simulated using the commercial software Aspen Plus® [50]. The system consists of a packed-bed column filled with unstructured packing as humidifier and a counter-current heat exchanger as dehumidifier. As to the humidifier, structured packing was also evaluated, but not further considered because leading to higher costs at similar performance (the comparison between structured and unstructured packing is discussed in detail in the Supplementary Material). The saline water is simulated by using the electrolyte Non-Random Two Liquid (eNRTL) model, which is suitable for electrolytes in an aqueous solution. Sodium chloride is assumed to be completely dissociated and always below its solubility limit. Concerning the dehumidifier, a generic air-water heat exchanger with constant heat transfer coefficient is considered.

The mass flow rate and temperature profiles along the HDH components are determined by solving the steady-state energy and mass balances for both humidifier and dehumidifier. The following assumptions are made:

- Constant radial profiles of velocity, temperature and concentration i.e. one-dimensional model along the axial direction z.
- Negligible air and water leakages.
- Negligible heat transfer resistance between condensed water and saline water in the dehumidifier, i.e. clean water is produced at the temperature of the saline water at the same location. This assumption is discussed by McGovern et al. and results in a discrepancy lower than 2% with respect to the actual fresh water temperature [24].

Fig. 2 shows a schematic representation of the process and highlights two differential control volumes within the humidifier (blue dashed line) and within the dehumidifier (red dashed line), as well as a control volume including a PVT module (green dashed line).

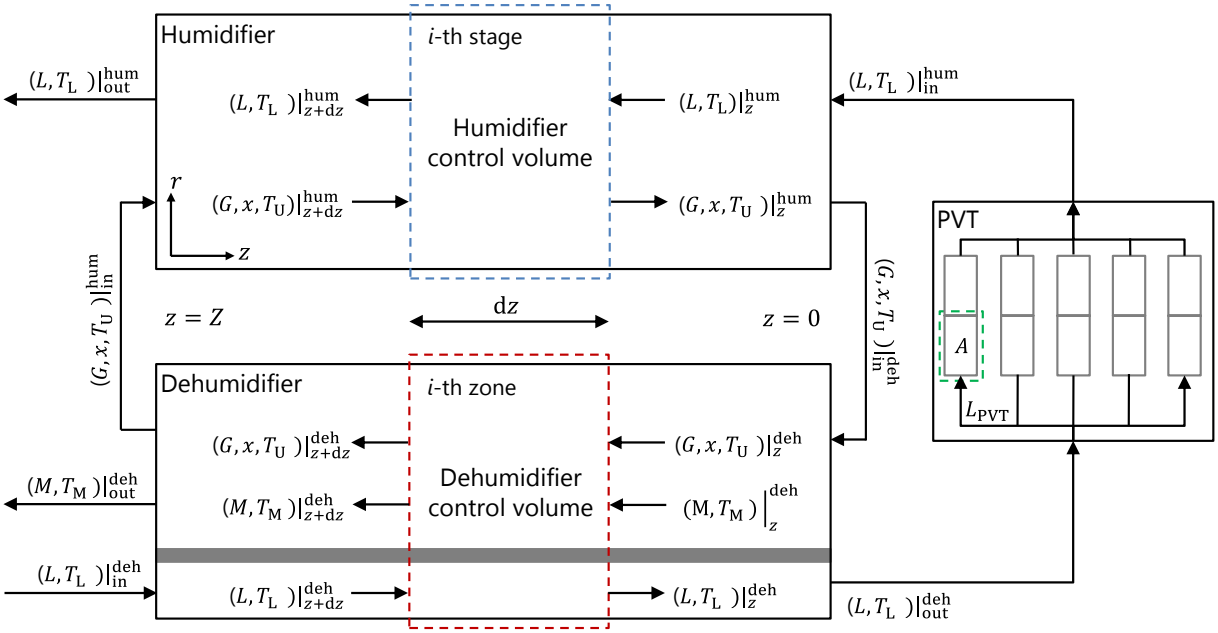

Fig. 2. Schematic of the HDH-PVT process and representation of two differential control volumes for both humidifier (blue dashed line) and dehumidifier (red dashed line), as well as the control volume including the PVT modules (green dashed line). (For interpretation of the references to colour in this figure legend, the reader is referred to the web version of this article.)

The following equations are written for a control volume of length dz within the humidifier:

- Material balances of saline water and moist air.

$$dL = JBdz \tag{2}$$

$$Gd\omega = JBdz \tag{3}$$

- Energy balances of saline water and moist air.

$$d(Lh_L) = FBdz \tag{4}$$

$$Gdh_U^* = FBdz \tag{5}$$

Here, L and G are the mass flow rates of saline water and dry air, respectively; ω is the humidity ratio (amount of water vapor per amount of dry air); B is a factor depending on the geometry of the column (i.e. $B = \pi D$ considering a cylindrical geometry with diameter D); J is the mass flux between water and air, determined by using the correlations proposed by Rocha et al. to calculate the mass transfer coefficient and interfacial area [51]; h is the specific enthalpy and h^* the specific enthalpy per amount of dry air; F is the heat flux between water and air, determined through the Chilton-Colburn analogy [52]. Note that the mass flow rate of dry air is constant in the entire HDH process, i.e. $dG/dz = 0, \forall z$, as only the water content of moist air, i.e. the humidity ratio ω, varies. Also, note that the air conditions at the inlet of the dehumidifier are those at the outlet of the humidifier and conversely.

In Aspen Plus®, a few parameters need to be chosen and calibrated to characterize the mass and heat transfer within the packed-bed column. These are the (i) packing type, (ii) column discretization, i.e. height of each stage, (iii) film discretization ratio, and (iv) flow model for liquid and vapor phases. Such parameters are derived by adopting established techniques for the calibration of radfrac numerical parameters [53–59]. They are reported in Table 1 and discussed in detail in the Supplementary Material. The diameter of the column is computed considering a vapor velocity that allows for reaching 80% of the flooding velocity along the column [46]. The value of the flooding velocity is provided by Aspen Plus based on the selected packing, which here is Flexiring by Koch-Glitsch [45]. Negligible heat losses are assumed.

The following equations are written for a control volume of length dz within the dehumidifier:

- Material balances of clean water and moist air.

$$dM = JBdz \tag{6}$$

$$Gd\omega = -JBdz \tag{7}$$

- Energy balances of water and moist air.

$$Ldh_L + d(Mh_M) = FBdz \tag{8}$$

$$Gdh_G^* = FBdz \tag{9}$$

Here, M is the mass flow rate of clean water; J is the mass flux of clean water condensing, which is driven by the difference in humidity ratio between the air stream and the saturation conditions; F is the heat flux between the air and the clean water, which is calculated by Aspen Plus® based on the properties of the fluid and by considering a constant heat transfer coefficient, a fixed fraction of heat losses and a fixed temperature pinch; the subscript M refers to clean water. Note that Eqs. 8 and 9 imply considering the thermal resistance between the moist air and the condensing water only, whereas the resistance between the clean and the saline water is neglected due to the high liquid-liquid heat transfer coefficient [24,47] (following the third assumption above). Moreover, note that the mass flow rate of saline water is constant along the dehumidifier ($dL/dz = 0, \forall z$) because of the indirect contact between air and water.

Similar to the humidifier, the following parameters need to be

calibrated in Aspen Plus® to characterize the dehumdifier: (i) temperature pinch, (ii) number of zones in which the heat exchanger is discretized, (iii) relative flow of water and air, (iv) heat losses as a fraction of the total duty. Based on this, the area of the heat exchanger is calculated by considering a constant heat transfer coefficient. The adopted values are reported in Table 1 and discussed in the Supplementary Material. Several values of the temperature pinch are considered to investigate the system design (see Appendix A). Pressure drops of 2 and 0.2 mbar/m^2 are assumed for water and air streams, respectively, across the HDH process. While such values are based on average values of pressure drops across the humidifier [45] and the dehumidifier [46], they only impact the auxiliary electricity consumption and do not affect the generality of the model.

While the simulation results of the HDH process are not validated experimentally, we believe that the software we adopted to model and simulate the HDH system – Aspen Plus®, Rate Based model – can accurately describe the phenomena happening in a packed tower in the conditions of interest. This was shown in literature for different, highly non ideal, water solutions [53–59].

2.2. Photovoltaic-thermal solar modules

PVT modules are conventional PV panels (either based on silicon or thin film technologies) integrated with a heat recovery system [60]. PV modules can convert only a limited fraction of the incident solar radiation into electrical power (between 10 and 20%), whereas a significant portion of the solar energy is dissipated in the form of heat. PVT collectors recover part of this heat, thus providing both electrical and thermal power [60,61]. A commercially available roll-bond PVT technology [48] is selected here due to the higher thermal efficiency with respect to the conventional sheet-and-tube technology [60,62,63]. In this case, the cooling fluid (saline water) passes through two metal sheets pressed against each other and forming a specific channel pattern. The thermal efficiency of the PVT modules, η_t, is calculated by using the following linear equation [64,65]:

$$\eta_t = \eta_o - \alpha \frac{T_{avg} - T_{amb}}{I} \tag{10}$$

where η_o is the optical efficiency and α a loss coefficient; T_{avg} is the average between inlet and outlet temperature of the cooling fluid, T_{amb} the ambient temperature and I the solar irradiance. Here, the value of I is modified to account for the incidence angle between the sun and the module. The term $(T_{avg} - T_{amb})/I$ is known as reduced temperature. The coefficients η_o and α, which are experimentally determined as discussed in the Appendix B by following the methodology and with the setup described in [60], are equal to $\eta_o = 0.50$ and $\alpha = 11.2$ W/(m^2 K). These translate in a thermal efficiency around 26% for a reduced temperature of 0.02 °C/(W/m^2). The experimental characterization of the PVT panels in real environmental conditions is motivated by the current lack of both standard testing procedure and data analysis for such technologies. Indeed, in authors' experience [60] and as shown in Appendix B, the performance provided by the manufacturer is often higher than the actual performance measured under realistic operating conditions.

The PVT modules can be connected both in series and in parallel, with the number of parallel- and series-connected modules being denoted as N_p and N_s, respectively (see, e.g., the scheme in Fig. 1 with $N_p = 5$ and $N_s = 2$); $N = N_p N_s$ is the total number of modules. The total water mass flow rate, L, is equally split among the modules connected in parallel; the resulting mass flow rate $L_m = L/N_p$ is the same for all modules. The following energy balance is written for all modules connected in series $i \in \{1, N_s\}$:

$$L_m c_p (T_{out,i} - T_{in,i}) = \eta_{t,i} I A \tag{11}$$

where A is the area of a PVT module; $T_{in,i}$ and $T_{out,i}$ the inlet and outlet temperatures of the i-th module, respectively; c_p the heat capacity at constant pressure of the saline water. Eqs. 10 and 11 can be rearranged to express the overall outlet temperature of the saline water as a function of the inlet temperature and the number of series-connected modules:

$$T_{out} = \phi^{N_s} T_{in} + \frac{\psi}{1-\phi}(1 - \phi^{N_s}) \tag{12}$$

where

$$\phi = \frac{2L_m c_p - \alpha A}{2L_m c_p + \alpha A}, \psi = \frac{2A(\eta_o I + \alpha T_{amb})}{2L_m c_p + \alpha A}$$

Note that while the coefficient ϕ depends on the design of the PVT installation and on the water properties only, the coefficient ψ varies with the ambient conditions. Eq. (12) states that the increase of water temperature across the PVT modules varies less than linearly with N_s due to increasing ambient losses.

The electricity generated by the PVT modules is calculated as [64]:

$$P = A N P^0 \frac{I}{I^0}[1 - \gamma(T_{cell} - T^0_{cell})] \tag{13}$$

where T_{cell} is the actual cell temperature; P^0, I^0 and T^0_{cell} are the standard electrical power, solar irradiance, and cell temperature, respectively. The standard electrical power is determined at standard test conditions ($I^0 = 1000$ W/m^2, $T^0_{cell} = 25$ °C); γ is the power coefficient. These parameters are available in the module datasheet [48].

The pressure drop across the PVT modules is computed by considering a quadratic increase with the water flow rate [48]:

$$\Delta p = \beta_1 L_m^2 + \beta_2 L_m \tag{14}$$

where β_1 and β_2 are constant coefficients provided by the manufacturer [48]. All the aforementioned parameters are reported in Table 1.

Finally, it must be noted that all the results discussed below are obtained by considering the aforementioned performance coefficients, i.e. η_o and α, which were determined experimentally for commercial PVT modules implementing aluminium for the hydraulic circuit. However, as the PVT-HDH system works with seawater as cooling fluid, an anti-corrosion material such as stainless steel should be considered. To do so, an assessment of the performance of a PVT with a stainless steel roll-bond heat exchanger is carried out with the help of a validated simulation tool [66]. Findings show that the thermal resistance of the heat exchanger material is negligible due to its small thickness and to the fact that heat transfer is limited by the contact resistance between roll-bond and PV module.

2.3. Performance indicators

The following indicators are defined to assess the technical performance of the desalination system:

i. Specific heat consumption, q [kWh/kg]. This is defined as the amount of total thermal energy required, Q, per unit clean water produced, W:

$$q = \frac{Q}{W} \tag{15}$$

Note that this is inversely proportional to the Gained-Output-Ratio (GOR), which is the ratio of the latent heat of evaporation of the distillate produced to the total heat input absorbed by the solar collectors. Conventional thermal desalination systems, such as multi-effect distillation (MED) or multi-stage flash (MSF), feature a specific thermal energy consumption ranging from 40 to 70 kWh/m^3 [67]. It is worth mentioning that, in a first approximation, for renewable-based technologies the specific energy consumption does not affect the operation cost.

ii. Specific electricity production, e [kWh/kg]. This is defined as the net amount of electrical energy generated, E, per unit clean water produced, W:

$$e = \frac{E}{W} \tag{16}$$

The net electricity is the difference between the electricity generated and that required by the auxiliary components, i.e. water pump and air fan. Note that for conventional technologies based on thermal modules the net electricity production is negative, as they only consume electricity.

iii. Specific fresh water production, w [$kg_{H_2O}/(hm^2)$]. This is the amount of produced clean water per unit solar area, A:

$$w = \frac{W}{AN} \tag{17}$$

The cost of clean water quantifies the economic performance of the desalination system. It is given by the ratio of the difference between the total cost of the system and the revenue gained by selling electricity to the grid to the amount of potable water produced:

$$c = \frac{K - pE}{W} \tag{18}$$

Here, K is the annual cost of the system; p is the electricity price; E and W are the net electricity generated and the clean water produced, respectively, during one year. A constant electricity price is considered. The total cost of the system includes the capital, installation and maintenance contributions. More specifically, installation costs are assumed to account for 50% of the capital cost of solar modules, inverter and HDH components, whereas maintenance costs are assumed to account for 5% of the overall capital cost. Such figures derive from personal communications with industry experts. The total cost is annualized by considering a discount rate of 7% and a lifetime of 25 years. With reference to the notation in Table 2, and by considering the standard expression of the annuity factor [68], K is expressed as

$$K = (1 + \lambda_{maint})[(1 + \lambda_{inst})(C_{HDH} + C_m + C_{inv}) + C_{BoP}]\frac{\delta}{1 - \frac{1}{(1+\delta)^{\tau}}} \tag{19}$$

where C is the total technology cost and the subscripts m and inv refer to the solar modules and the inverter, respectively. Note that while the unit capital costs of the components of the solar system are constant with the size, the nonlinear correlation proposed by Brunazzi et al. is used to calculate the cost of the humidifier as function of the column diameter and height [69]. All the parameters required for the calculation of the system cost are reported in Table 2, together with the relevant references. Whereas all economic assumptions are relatively general, i.e. the costs of the components do not reflect any specific geographic location, the discount rate of 7%, together with a constant electricity price, are considered to be representative of the applications of interest [70,71].

Table 2
Economic parameters used for techno-economic assessment.

Unit capital cost of PVT modules	1600 €/kW_e (based on [72,48])
Unit capital cost of PV modules	550 €/kW_e [72]
Unit capital cost of thermal modules	350 €/kW_t [73]
Unit capital cost of inverter	300 €/kW_e [72]
Unit capital cost of humidifier packing	200 €/m^3 [69,46]
Unit capital cost of humidifier tower	$f(D, H)$ [69]
Unit capital cost of dehumidifier	0.7 €/(kg/h) of treated water [30]
Fixed balance-of-plant (BoP) costs	2500 € [74]
Installation costs, λ_{inst}	50% of capital cost of solar and HDH units [74]
Maintenance costs, λ_{maint}	5% of total capital cost [74]
Lifetime of the system, τ	25 a [74]
Discount rate, δ	7% [70,71]

3. Results and discussion

A PVT-HDH process operating at ambient pressure and treating brackish water at 20 °C with a salt mass concentration of 20 g/l is investigated, for the range of design and operating conditions summarized in Table 3. The results section proceeds as follows. First, the optimal design of the system is investigated for a wide range of ambient conditions by evaluating the impact of saline water flow rate, PVT configuration and HDH size on the amount of clean water produced. Next, the optimal operation of the system is characterized as function of the ambient conditions for a fixed system design. Finally, a techno-economic assessment is carried out to compare the proposed technology against conventional solar-driven HDH units.

Table 3
Design and operation variables, with corresponding ranges of the sensitivity analysis.

Design variables	
Number of series-connected PVT modules	1–4
Height of humidifier (size of HDH system)	3.6–6.4 m
Operating pressure	1.01 bar
Operation variables	
Saline water flow rate through a PVT module	0.5–2 l/min
Ambient conditions	
Ambient temperature	15–45 °C
Solar irradiance	200–1000 W/m^2

As mentioned above, we consider a balanced HDH system, which minimizes the energy losses by operating at the optimal water-to-air mass flow rate ratio given by Eq. (1) [16–19]. In this case, the PVT-HDH system is characterized by one control variable only, since the flow rate of saline water determines that of moist air, and conversely. This implies that, for fixed system design and conditions of the saline water, fixing the flow rate of one fluid allows defining the process temperatures and thus the process performance.

3.1. Design considerations

Concerning the aforementioned control variable, here we act on the saline water flow rate and we perform a sensitivity analysis aimed at determining its optimal values, which lead to the maximum amount of clean water produced, for several ambient conditions (see Table 3). The range of flow rate is defined by the minimum and maximum flow rates through a single PVT module, namely 0.5 and 2 l/min, respectively [48]. Furthermore, the optimal system design is studied in terms of (i) series–parallel configuration of the PVT modules, and (ii) size of the HDH system. The former is studied by varying the number of series-connected modules from 1 to 4, while keeping the same value of total solar area. The latter, which characterizes the HDH performance in terms of heat and mass transfer, can be described by referring only to the height of the humidifier, H, since a balanced system is considered. Indeed, the area of the dehumidifier is defined by the condition of equal enthalpy losses within humidifier and dehumidifier [16–18]. Here, H varies between 3.6 and 6.4 m, which are considered reasonable values for the scale of interest. In the following, the state of the system is represented by the maximum process temperature, i.e. at the outlet of the PVT modules and inlet of the humidifier.

3.1.1. Effect of saline water flow rate on clean water produced

The results obtained when varying the mass flow rate of treated saline water are illustrated in Fig. 3-a for different values of solar irradiance, I, and a fixed ambient temperature T_{amb} = 30 °C. The figure shows the specific mass flow rate of clean water, w (solid lines), and the maximum process

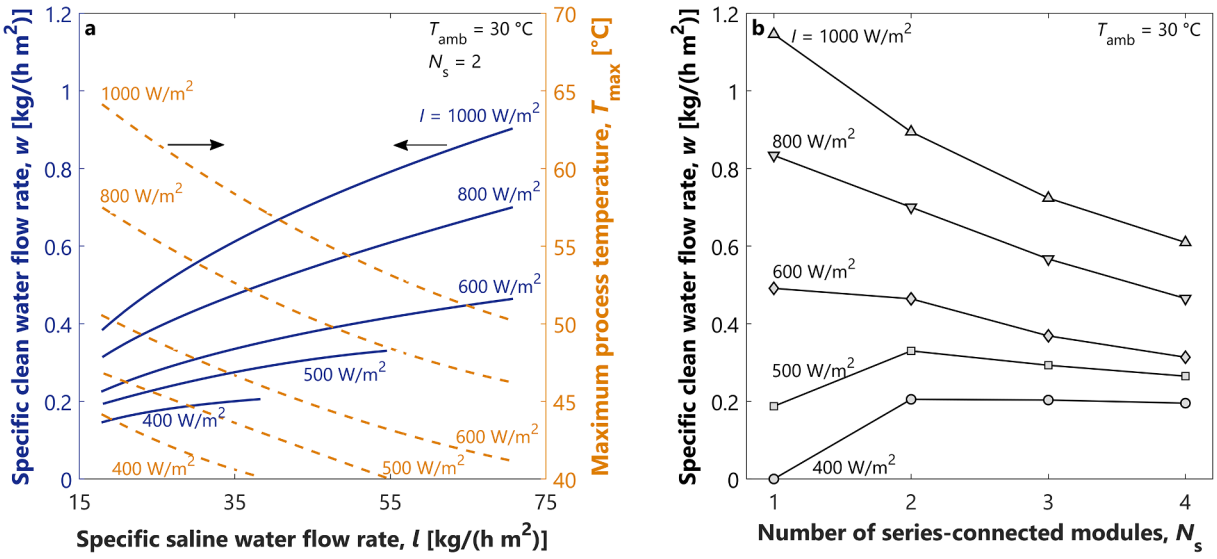

Fig. 3. a) Specific mass flow rate of clean water (solid lines) and maximum process temperature (dashed lines) as function of specific mass flow rate of saline water, for varying solar irradiance I = 400, 500, 600, 800, 1000 W/m² and for N_s = 2, i.e. two series-connected modules. b) Maximum clean water production for different PVT configurations featuring N_s = 1 − 4 and for varying solar irradiance. T_{amb} 30 °C, H = 3.6 m.

temperature, T_{max} (dashed lines), as function of the specific mass flow rate of saline water, l, for a PVT configuration featuring two series-connected modules, N_s = 2. The water flow rates are expressed per unit area of solar modules. For a fixed humidifier height, this is equivalent to expressing them per unit area of humidifier section, as the ratio of column area to solar area is constant; for H = 3.6 m this ratio is equal to r = 0.004. One can note that the amount of clean water produced increases with the saline water flow rate, whereas the maximum process temperature decreases. This is because higher water and air flow rates and lower energy losses are predominant over the lower air humidity ratio obtained at lower process temperatures. In other words, for given solar irradiance I the amount of fresh water produced is maximized by working at the maximum value of saline water flow rate, corresponding to the minimum value of maximum process temperature. At the same time, a low value of T_{max} is beneficial for the PVT modules in terms of electrical efficiency and therefore of electricity generation. Similar considerations can be made when varying the ambient temperature T_{amb} (T_{amb} and I within the ranges defined in Table 3). This suggests that the system is optimally operated by working at the highest feasible value of l, which results in the lowest feasible value of T_{max}.

The maximum value of saline water flow rate is determined by the PVT modules, while the minimum value of maximum process temperature is determined by the HDH system. For the configuration investigated in Fig. 3-a, no clean water is produced for values of maximum process temperature below 40 °C, as the differences between inlet and outlet temperatures of humidifier and dehumidifier are too small. This means that below a certain value of ambient temperature and solar irradiance the clean water production is constrained by the minimum value of T_{max}. In this case, the saline water flow rate is set at the maximum possible value within the feasible range so as T_{max} = 40 °C. On the contrary, above certain threshold values of ambient temperature and of solar irradiance the clean water production is constrained by the maximum value of l. In this case, the saline water flow rate through a PVT module is equal to 2 l/min and T_{max} increases with I and T_{amb}.

3.1.2. Effect of PVT configuration on clean water produced

The impact of the number of series-connected modules on the clean water production is shown in Fig. 3-b. Increasing N_s translates in higher values of temperature difference across the solar installation, but lower values of saline water mass flow rate. On the one hand, with N_s = 1 the performance of the system is maximized at high values of solar irradiance. However, in this case the production of clean water drops drastically at low values of solar irradiance, where a very limited energy input is provided by the PVT. In specific, no water is produced below 400 W/m² because a maximum process temperature of 40 °C cannot be reached even when working at the lowest level of saline water flow rate. On the other hand, a higher N_s allows transferring more heat to the saline water, which allows working in a wider range of solar irradiance values. In this case, a smaller amount of saline water is treated per unit solar area. This leads to a lower clean water production at high values of I, but to a higher clean water production at low values of I. For 400 ⩽ I ⩽ 500 W/m², N_s = 2 maximizes the production of clean water, leading to a significant improvement with respect to N_s = 1. For I ⩾ 600 W/m², the disadvantage of using N_s = 2 is much limited compared to N_s > 2. Therefore, N_s = 2 is selected as the optimal trade-off between system performance and flexibility within the range of ambient conditions of interest, and is considered hereafter. Again, similar considerations can be made for the ambient temperature.

3.1.3. Effect of HDH geometry on clean water produced

The impact of the HDH geometry, represented by the humidifier height, on the clean water production is presented in Fig. 4, which

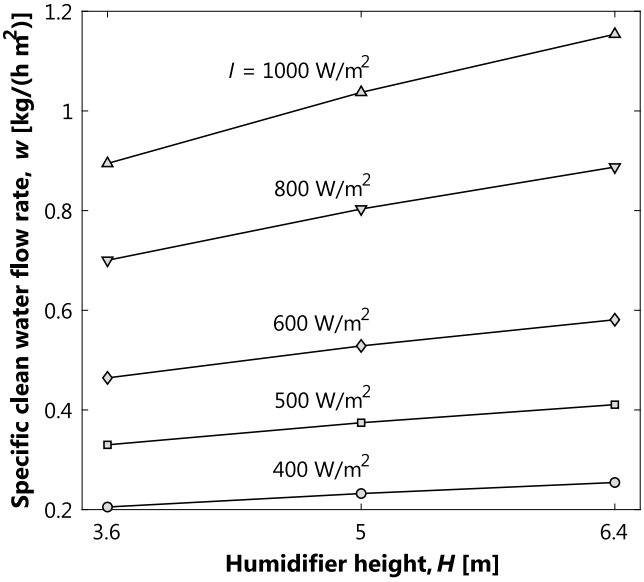

Fig. 4. Specific mass flow rate of clean water as function of humidifier height for varying solar irradiance I = 400, 500, 600, 800, 1000 W/m². N_s = 2, T_{amb} = 30 °C.

shows the specific mass flow rate of clean water as function of the humidifier height for different values of solar irradiance, at a fixed ambient temperature of 30 °C. A taller humidifier allows increasing the effectiveness of heat and mass transfer (i.e. it allows reducing the energy losses across the HDH process, as shown in Appendix A, Fig. 9), hence permitting to reduce the thermal energy consumption. Consequently, the specific water production increases for higher H, with an improvement of about 25% when going from $H = 3.6$ m to $H = 6.4$ m. In the following, a humidifier height of $H = 3.6$ m is considered to illustrate the system performance, but similar considerations apply to different values of H.

3.2. Optimal operating regions

Based on the results of the previous section, reference values are selected for the saline water flow rate (i.e. the control variable of the system), the PVT configuration, and the HDH size (i.e. relevant design quantities). More specifically, the optimal value of l for each ambient condition, $N_s = 2$, and $H = 3.6$ m are selected. Based on such design features, the optimal system operation as function of ambient conditions is illustrated in Fig. 5, which reports the behavior of (a) optimal maximum temperature, (b) clean water production, (c) thermal energy consumption, and (d) electrical energy production on a $T_{amb} - I$ plane, spanning the ranges of ambient conditions of interest. In the following, we use as reference ambient temperature and solar irradiance those reported for Abu Dhabi (see Fig. 3 of reference [43]), where a typical day with hour resolution is considered for each month of the year; the ambient temperature and solar irradiance of a typical day of April are indicated by the red dots in Fig. 5. Three distinct regions are identified on the $T_{amb} - I$ plane: (i) an unfeasible region (grey-shaded) at low ambient temperature and solar radiation, where no fresh water is produced; (ii) a constant temperature region (blue-shaded, Fig. 5-a), where the system is operated at 40 °C, independently of the ambient temperature and solar radiation, and produced fresh water, consumed heat and produced electricity vary according to the ambient conditions; (iii) a region where all the variables vary according to the ambient conditions, and they are constrained by the maximum value of saline water flow rate. One can note that for ambient conditions outside the

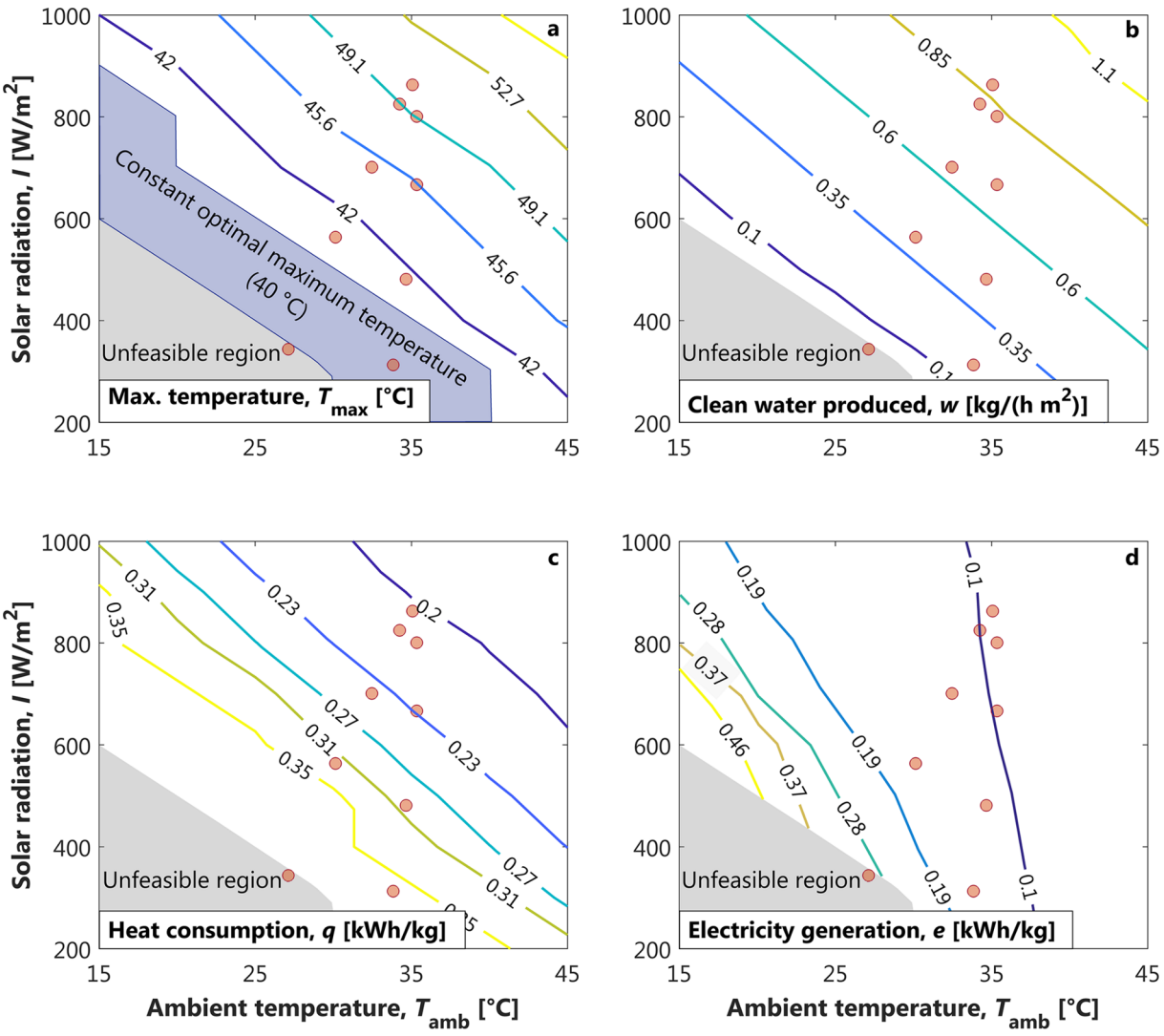

Fig. 5. Optimal state and performance of the PVT-HDH system as functions of ambient conditions, namely ambient temperature, T_{amb}, and solar irradiance, I. The optimal state of the system is represented by the maximum process temperature (a); the optimal performance is reported in terms of (b) specific mass flow rate of produced clean water, (c) thermal energy consumption per unit clean water produced, (d) electrical energy production per unit clean water produced. Three regions are identified: (i) unfeasible region (grey-shaded), (ii) constant temperature region (blue-shaded), where the other variables vary according to the ambient conditions (isolines), (iii) a region where all variables vary according to the ambient conditions (isolines). Simulations are performed with a step of 5 °C for the ambient temperature and 100 W/m^2 for the solar irradiance; this reflects on the shape of the unfeasible region. The reference values of hourly-resolved ambient temperature and solar irradiance (only for $I > 200$ W/m^2) are indicated by red dots [43]. $N_s = 2, H = 3.6$ m. (For interpretation of the references to colour in this figure legend, the reader is referred to the web version of this article.)

unfeasible region the fresh water production increases with T_{amb} and I. Furthermore, the specific thermal energy exhibits a behavior directly connected to that of the maximum process temperature and to that of produced clean water, whereas the net electricity generation depends on the variation of the PVT electrical efficiency with T_{amb} and I (see Eq. (10)) and of the produced clean water. Lower specific heat consumption and electricity production are observed at high T_{amb} and I, since the consumed and generated energy increase slower than the water production with the ambient conditions.

3.3. Techno-economic assessment

In the following, a techno-economic assessment of the PVT-HDH system is carried out to identify the conditions at which the proposed system is convenient with respect to HDH processes driven by conventional solar technologies. First, the yearly productions of clean water and electricity are assessed for different solar-driven technologies, and the total cost of clean water is calculated. Then, the effects of electricity price, ambient conditions, amount of yearly water produced and size of the HDH process on the cost of clean water are evaluated.

3.3.1. Cost of clean water

The analysis starts from the calculation of the yearly water and electricity production, which are determined by using the profiles of ambient temperatures and solar irradiance given in [43] and reported in Appendix C for convenience. Based on such ambient conditions, the PVT-HDH system is operated following the optimal behavior discussed in Section 3.2. The resulting water production is illustrated in Fig. 6, which shows (a) the hourly profiles of clean water produced for the average April, July, and December days, and (b) the daily clean water production for the average day of each month of the year. As expected, the water production always reaches its maximum during the central hours of the day, where the highest values of ambient conditions are registered. Moreover, whereas the fresh water production is similar during mid-season months, the water produced in winter is only about 10% of that produced in summer. The average water production per unit solar area over the entire year is about 0.2 kg/(h m^2). The average heat consumption and electricity production per unit clean water produced over the entire year are about $q = 0.34\,kWh_t/kg$ and $e = 0.15\,kWh_e/kg$, respectively. It is worth mentioning that the high heat consumption is due to the single-stage HDH configuration considered in this work [26,27]. Values closer to those typical of conventional systems, in the range of $q = 0.05–0.1\,kWh_t/kg$, can be obtained by adopting multi-stage configurations. In fact, values of specific heat consumption as low as $0.12\,kWh_t/kg$ [2] can be achieved by optimizing the process, which is beyond the scope of this work. Furthermore, it is worth noting that the low average water production results in a large solar area: For example, a total water production of 365 m^3/y (500 people using 2 liters of clean water per day) requires a solar area of about 210 m^2. While this value can be reduced by optimizing the process according to the reduction in energy consumption, it confirms that HDH processes are not suited for the production of large volumes of clean water.

The same calculation is performed for different systems that adopt conventional solar technologies as energy source of the HDH process. In particular, thermal collectors (Th) [49] and a combination of thermal and PV modules (Th + PV, hybrid system) [48] are investigated. Conventional flat-plate, sheet-and-tube thermal collectors are selected. They are characterized by a higher optical efficiency and a lower thermal loss coefficient than PVT modules, resulting into a thermal efficiency ranging from 0.4 to 0.7 (about twice that observed for the PVT technology). Consequently, they can operate within a larger range of water flow rate (from 1.25 l/min to 8.3 l/min) and therefore within a wider span of ambient conditions (e.g. solar radiation as low as 200 W/m^2). Concerning the configuration with both thermal collectors and PV panels, the area of thermal and PV modules is such that the total solar area of the system equals that of the PVT system per unit clean water produced. A configuration with two-series connected modules is considered for all solar modules, as this represents the optimal trade-off between system performance and flexibility for the reference ambient conditions. For each system, the same HDH process featuring a height of $H = 3.6$ m is considered. The main performance indicators for the three configurations at the reference ambient conditions are summarized in Table 4. Because of the higher performance and flexibility, thermal collectors lead to a greater water production per unit of solar area than PVT modules. However, simply adopting thermal collectors does not allow to generate electricity and requires an external power source to run the auxiliaries. Similarly, the hybrid configuration features an electricity generation of about 50% that of the PVT-based system per unit clean water produced.

Based on such performance and on the economic assumptions

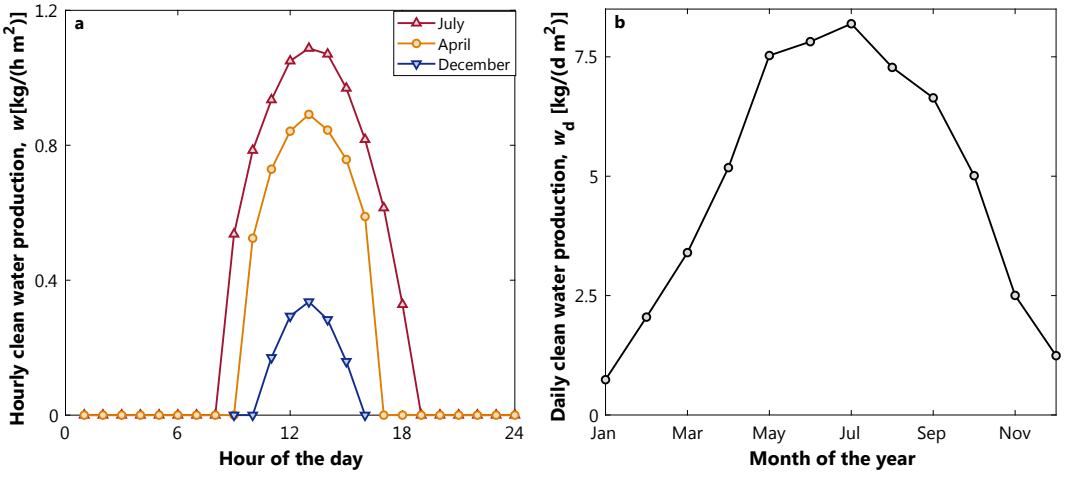

Fig. 6. a) Hourly profiles of specific clean water mass flow rate for an average day in April (squares), July (circles), and December (diamonds). b) Daily produced clean water during the average day of each month of the year. $N_s = 2$, $H = 3.6$ m.

Table 4
Performance indicators for the investigated systems at the reference ambient conditions.

	PVT	Th	Th + PV
Average water production, [kg/(hm^2)]	0.2	0.46	0.21
Average thermal consumption, [kWh$_t$/kg]	0.34	0.34	0.34
Average net electrical production, [kWh$_e$/kg]	0.15	−0.007	0.07

reported in Table 2, the cost of clean water is determined for all the considered solar-driven HDH processes. As mentioned above, although the economic assumptions are relatively general, a discount rate of 7% and a constant electricity price (both for buying and selling) are consistent with the selected ambient conditions for Abu Dhabi and with the applications of interest [70,71]. Concerning the PVT-based system, the solar modules give the major contribution to the overall installation cost, around 35%, while the HDH contribution is of about 20%. However, while humidifier, dehumidifier and inverter are off-the-shelf units and significant cost reductions are not expected, PVT modules constitute a fairly novel technology and a learning curve leading to reduced costs can be envisioned [75]. Similar considerations apply to thermal and PV panels, although currently they are significantly cheaper than the PVT modules and account for a smaller share of the cost of the corresponding clean water.

The cost of clean water given by Eq. (18) is the difference between two terms: the specific annual cost $k = K/W$ and the specific annual revenue $e = pE/W$. The former depends on the amount of clean water produced because water production increases faster than the capital cost: while water production increases linearly, installation cost increases less than linearly due to the contribution of fixed costs and to the nonlinear cost of humidifier. The latter is independent of the water production, as E scales proportionally with W, but it depends on the electricity price, p. Furthermore it is noted that, similar to the system performance (see Fig. 4), the system cost increases with the height of humidifier, with the cost of clean water being a trade-off between these two effects.

3.3.2. Effect of electricity price on cost of clean water

First, we investigate the effect of electricity price on the cost of clean water for a fixed yearly water production, a fixed humidifier height, and reference ambient conditions. This is illustrated in Fig. 7-a, which shows the cost of clean water, c, as a function of the electricity price, p, for all the considered systems. Four different regions of electricity price are identified:

- *Lower range*, $p < p_*$. For an electricity price below a certain threshold p_*, the most convenient solution is a system implementing solely thermal collectors. In this case, the system is a conventional solar-driven desalination unit, which buys from the grid the electricity needed for the auxiliaries.
- *Intermediate range*, $p_* < p < p^*$. For an electricity price varying within p_* and p^*, the most convenient solution is a hybrid system implementing a combination of thermal and PV modules. In this case, the system produces both the heat and the electricity required by the HDH process and provide electricity to an end-user.
- *Higher range*, $p > p^*$. For an electricity price above a certain threshold p^*, the most convenient solution is a system implementing PVT modules, which produces about twice the electricity produced by the hybrid system per unit solar area.
- *Negative cost range*, $p > p^0$. For an electricity price above a certain threshold $p^0 = k/e$, the cost of the PVT-based system is negative, as the revenue made by selling electricity to an end-user is larger than the annual cost. Note that the specific annual cost of the system, k, is equal to the cost of clean water when the electricity price is zero. A similar electricity price threshold, greater than p^0, exists for the hybrid system, while this does not hold for the system driven by thermal collectors.

This makes the PVT-HDH system a very promising technology for water desalination in remote areas (e.g. Sub-Saharan Africa), where the price of off-grid electricity can easily go up to 0.25 €/kWh, i.e. it can be larger than reasonable values of p^* and p^0 [76]. Again, it is worth mentioning that the high cost of clean water depends on the single-stage HDH configuration adopted in this work. Optimized thermal solar-driven HDH cycles are characterized by a water cost in the range of 3–5.5 €/m^3 (due to the reduced heat consumption) [2]. This suggests that all the curves reported in Fig. 7 can be translated downwards when optimizing the HDH process.

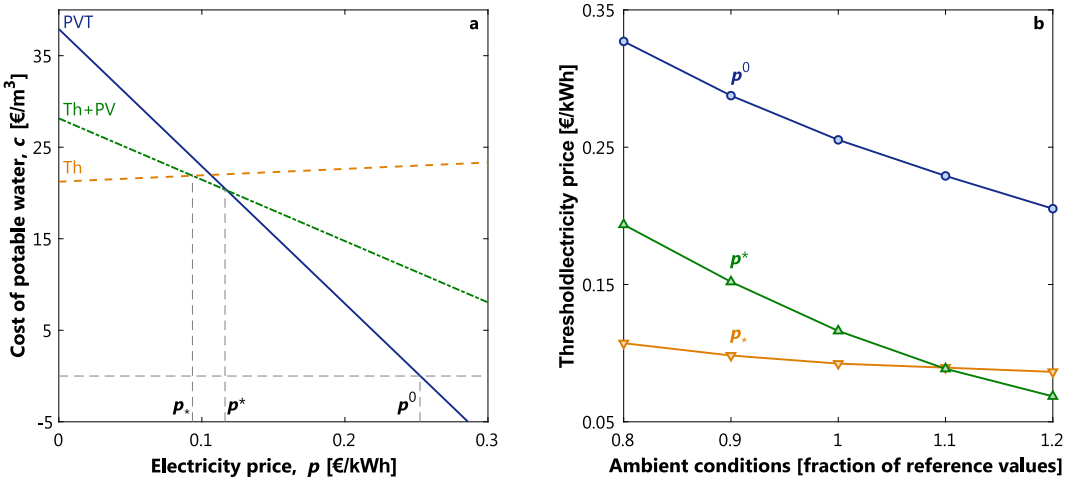

Fig. 7. a) Specific cost of clean water as function of electricity price for different systems implementing PVT modules (blue solid line), thermal collectors (Th, yellow dashed line) and a combination of thermal and PV modules (Th + PV, green dash-dotted line) for reference ambient conditions. Four different regions of electricity prices are identified: (i) $p < p_*$, where the Th configuration is the most convenient; (ii) $p_* < p < p^*$, where the Th + PV configuration is the most convenient; (iii) $p > p^*$, where the PVT configuration is the most convenient; (iv) $p > p^0$, where the PVT configuration results in negative costs. b) Impact of variation of ambient conditions on the thresholds of electricity price. $N_s = 2$, $H = 3.6$ m, $W = 200$ m^3/y. (For interpretation of the references to colour in this figure legend, the reader is referred to the web version of this article.)

3.3.3. Effect of ambient conditions on cost of clean water

The impact of the ambient conditions on the electricity price thresholds defined above is presented in Fig. 7-b. The ambient conditions are varied by keeping the reference profiles of ambient temperature and solar irradiance and by changing their values from 80% to 120% of the reference values. One can note that the lower range threshold, p_*, remains fairly constant independently of the ambient conditions. On the contrary, the upper range threshold, p^*, decreases significantly for higher ambient conditions. This implies that the intermediate range, where the hybrid system is the most convenient solution, increases at low ambient conditions, whereas it disappears at high ambient conditions, where the PVT modules are the most cost-effective option in a wider region of electricity prices. Overall, the PVT-based system is less convenient at low ambient conditions, due to (i) a greater deterioration of the performance with respect to the thermal collectors, and (ii) a reduced impact of electricity generation. Similarly, the negative cost threshold, p^0 decreases at high ambient conditions. In other words, lower ambient conditions require a higher electricity price to compensate for the capital and maintenance costs, as a lower electricity production is obtained for the same system size.

3.3.4. Effect of amount of water produced on cost of clean water

The impact of water production on the electricity price thresholds is presented in Fig. 8-a. The water production is varied from 200 to 1000 m^3/y, which covers the range of interest for the considered application with an installed solar area ranging from 115 to 570 m^2 (considering $w = 0.2$kg/(h m^2) for the reference ambient conditions). Again, note that these values of solar area can be reduced by optimizing the HDH process [2]. The upper price threshold, p^*, is independent of W. This implies that, independently of the water production, the PVT-based system represents the most cost effective solution above a certain electricity price, about 0.11 €/kWh for the conditions considered in Fig. 8. In this case, the higher electricity generation compensates the lower thermal performance of the PVT compared to thermal modules. On the contrary, the lower price threshold, p_* decreases with the water production, which means that the hybrid system is more convenient at higher values of W.

3.3.5. Effect of HDH size on cost of clean water

Finally, the effect of the humidifier height on the cost of clean water produced by the PVT-based technology is studied. More specifically, the cost of clean water is calculated as function of the water production for three different heights of the humidifier, namely $H = 3.6$, 5, and 6.4 m (the behavior is shown in Appendix D). Similar to the thresholds of electricity price defining the most convenient solar-based technology, we determine values of price that define the most convenient humidifier height. These are denoted as p_5^*, the threshold electricity price above which $H = 5$ m is more convenient than $H = 3.6$ m, and $p_{6.4}^*$, the threshold electricity price above which $H = 6.4$ m is the most convenient technology. Of course, the generality of such analysis is not affected by the selected values of H. Such thresholds as function of the yearly water production are shown in Fig. 8-b, which indicates the most convenient humidifier height on the (W, p) plane. Taller humidifiers are more convenient at higher yearly water productions and lower electricity prices, for which the improvement in system performance is predominant over the increase in system cost.

4. Conclusions

This work analyzes the performance of an HDH system coupled with PVT solar modules for the simultaneous cogeneration of clean water and electricity. The optimal design and operation of the process are investigated, and a techno-economic assessment is carried out to evaluate the cost of the clean water produced.

Being constituted of established technologies, namely a packed-bed column as humidifier and an air–water heat exchanger as dehumidifier, the HDH system is simulated through a commercial software accounting for detailed heat and mass transfer limitations. On the contrary, being a relatively new technology, with no established testing procedure, PVT modules are investigated experimentally to characterize the simultaneous generation of electricity and heat under realistic operating conditions. Such characterization is then used in the process model.

Based on the maximum-efficiency ratio of water to air mass flow rates, the optimal design of the system is determined for a wide range of ambient conditions by evaluating the impact of saline water flow rate,

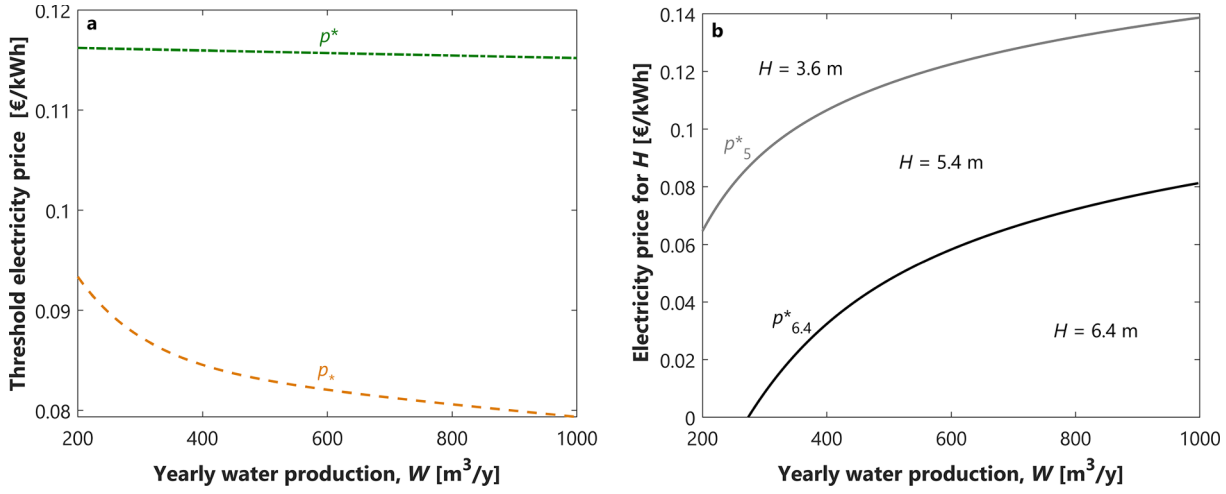

Fig. 8. a) Impact of water production on the thresholds of electricity price. b) Impact of water production on the thresholds of electricity price defining the most convenient height of humidifier. Reference ambient conditions, $N_s = 2$, $H = 3.6$ m.

PVT configuration, and HDH size on the amount of clean water produced. Furthermore, the optimal operation of the system is characterized as function of the ambient conditions for a fixed system design. The state of the system is represented by the maximum process temperature, at the outlet of the PVT modules, whereas the performance is evaluated in terms of clean water and electricity generation. The water production is maximized when operating at the highest possible saline water flow rate, which results in the minimum possible temperature at the outlet of the PVT modules. Such values depend on the PVT configuration and on the ambient conditions. A configuration with two series-connected solar modules represents the optimal trade-off in terms of system performance and flexibility, maximizing the water production along the year for the selected ambient conditions.

Furthermore, the cogeneration of clean water and electricity is assessed from a techno-economic perspective by evaluating the total cost of clean water and by comparing this against that of conventional solar-driven HDH processes, which implement thermal and photovoltaic panels, for a wide range of electricity prices, ambient conditions, yearly water production and HDH size. Findings show that different solar technologies are economically convenient for different regions of electricity price, with thermal collectors being the cost-optimal solution at low electricity prices and PVT modules being the cost-optimal solution at high electricity prices. Furthermore, when electricity is generated, the cost of clean water becomes negative above certain values of electricity prices. For values of electricity price typical of developing countries, PVT-based HDH systems represent the cost-optimal solution, and can deliver clean water at a negative cost. In fact, such price regions depend on the ambient conditions, the yearly water production, and the HDH size. Whereas the PVT technology leads to expensive clean water at low ambient conditions, its high electricity production makes it the cheapest solution at high ambient conditions. Similarly, higher electricity prices are required at low ambient conditions to compensate the investment costs and obtain a negative cost of clean water. Moreover, taller humidifiers are more convenient at higher yearly water productions and lower electricity prices, for which the improvement in system performance is predominant over the increase in system cost.

Declaration of interests

None declared.

Appendix A. Numerical method

The numerical procedure adopted in this work to simulate the PVT-HDH process is presented in the following. The inputs to the simulation are (i) saline water inlet temperature and salinity; (ii) maximum process temperature; (iii) height of the humidifier and parallel-series configuration of the PVT modules; (iv) ambient conditions, namely ambient temperature and solar irradiance; (v) PVT performance characteristics. Based on these, the model determines (i) flow rates of clean water, saline water and air; (ii) thermal energy consumption; (iii) electrical energy consumption and production.

First, the HDH process is simulated in Aspen Plus® to investigate the effectiveness of the mass and heat transfer. This is given in terms of enthalpy pinch Ψ, which is the difference between the specific enthalpy of the inlet fluid and that of the outlet fluid if they were at the same temperature, and represents the minimum loss in specific enthalpy due to the finite size of the device. Here, the minimum-entropy condition given by Eq. (1) is assumed. In this case, the system is said to be thermodynamically balanced and the enthalpy pinch is equal for humidifier and dehumidifier, i.e. $\Psi^{deh} = \Psi^{hum} = \Psi$. For a balanced system, and for a given type of humidifier and dehumidifier (see Section 2), Ψ is a function of the height of the humidifier H and the maximum process temperature T_{max}. This is shown in Fig. 9, which reports the enthalpy pinch as a function of the maximum process temperature (inlet temperature of the saline water in the humidifier) for three different humidifier heights. Both the Aspen Plus® simulation points and the corresponding quadratic fitting are reported. The following quadratic fitting is determined:

$$\Psi = -16.9 + 6.22H + 0.20T_{max} - 0.09H^2 - 0.15HT_{max} + 0.01T_{max}^2 \quad (20)$$

Note that for a balanced system, the enthalpy pinch also determines the size (i.e. area) of the dehumidifier.

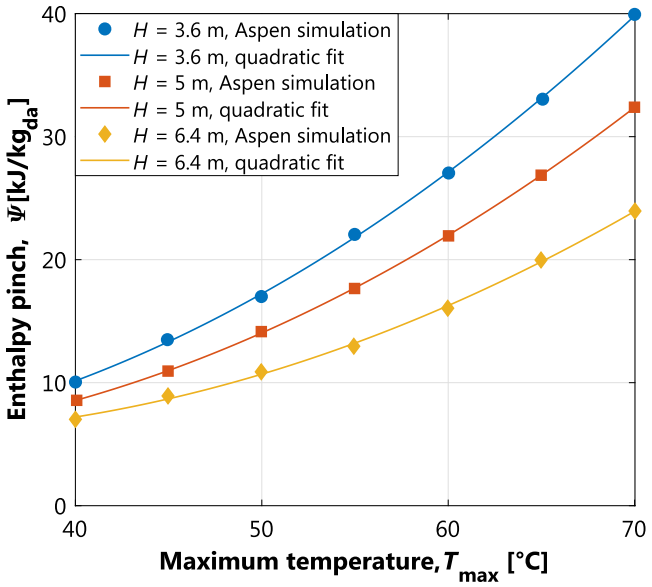

Fig. 9. Enthalpy pinch as function of the maximum process temperature for three different heights of the humidifier, namely H = 3.6, 5 and 6.4 m. Simulation points and quadratic fit.

Once Ψ is determined, it is used to quantify the mass and heat transfer within the following procedure, which is based on previous work from Chehayeb et al. [26]:

i. The enthalpy of the air at the outlet of the dehumidifier is calculated as

$$h^*_{U,out} = h^*_U(T_{L,in}) + \Psi \tag{21}$$

ii. The enthalpy of the air at the inlet of the dehumidifier is computed by assuming a guess value of the specific enthalpy variation Δh^*:

$$h^*_{U,in} = h^*_{U,out} + \Delta h^* \tag{22}$$

Since saturated air is always assumed, the specific enthalpy, h^*_U, and the absolute humidity ω of the air are known at every location of the cycle.

iii. The enthalpy profiles along the HDH process are determined by solving the set of Eqs. (2)–(9), where the mass and heat fluxes are eliminated, being the mass and heat transfer described by Ψ. In particular, the following set of dimensionless equations is solved:

$$\begin{aligned} &\frac{d\phi}{d\zeta} = \frac{d\omega}{d\zeta} \\ &\Omega\frac{d\theta}{d\zeta} = \frac{d\theta^*}{d\zeta} - \frac{d\phi\theta}{d\zeta} \\ &\frac{d\mu}{d\upsilon} = \frac{d\omega}{d\upsilon} \\ &\frac{d(\mu\xi)}{d\upsilon} = \frac{d\xi^*}{d\upsilon} \end{aligned} \tag{23}$$

with the following boundary conditions:

$$\begin{aligned} &\phi(\zeta = 0) = 0 \\ &\theta(\zeta = 1) = 1 \\ &\mu(\upsilon = 0) = \Omega \\ &\xi(\upsilon = 0) = 1 \end{aligned} \tag{24}$$

where the following dimensionless variables are introduced:

$$\begin{aligned} &\phi = \frac{M}{G}, \quad \mu = \frac{L^{hum}}{G} \\ &\theta = \frac{h_L^{deh}}{h_L^{in,deh}}, \quad \theta^* = \frac{h_U^{*deh}}{h_L^{in,deh}} \\ &\xi = \frac{h_L^{hum}}{h_L^{in,hum}}, \quad \xi^* = \frac{h_U^{*hum}}{h_L^{in,hum}} \\ &\zeta = \frac{z}{H^{deh}}, \quad \upsilon = \frac{z}{H^{hum}} \end{aligned} \tag{25}$$

where $h_L^{in,deh}$ is the specific enthalpy of saline water entering the dehumidifier and is an input to the simulation process; $h_L^{in,hum}$ is the specific enthalpy of saline water entering the humidifier and is an input to the simulation process (calculated from T_{max}); ω and h^*_U are known along the whole process once Δh^* is chosen; H^{deh} and H^{hum} are the length of the dehumidifier and humidifier, respectively. The choice of Δh^* also allows to determine Ω through Eq. (1).

iv. The enthalpy pinch of the humidifier is computed. If this is not equal to the starting value (i.e. the enthalpy pinch of the dehumidifier), the value of Δh^* is updated and the steps i-iii repeated. The simulation completes when the discrepancy between the humidifier and dehumidifier pinch is lower than a tolerance, fixed at 0.001 kJ/kg_{da}.

v. Then, the temperatures of the saline water at the inlet and outlet of the PVT modules are used in Eq. (11), together with ambient conditions and thermal efficiency of the modules, to determine the mass flow rate of saline water across the dehumidifier.

vi. Finally, the mass flow rates of dry air is given by

$$G = \Omega L^{deh} \tag{26}$$

and the total produced clean water W is calculated as

$$W = \phi(\zeta = 1)G \tag{27}$$

Appendix B. Experimental characterization of PVT panels

The electrical and thermal performance of the PVT modules are identified here by γ (see Eq. (13)) and η_t (see Eq. (10)). However, being PVT modules a relatively new technology, no directive is set for the assessment of electric and thermal performance. For commercial modules, the electric

and thermal performance are typically evaluated independently by means of two different tests: (i) The electric characteristic is determined through a flash test at Standard Test Conditions (STC), namely $I = 1000\,W/m^2$ and $T_{cell} = 25\,^{\circ}C$ (Solar Flash Tests, or Sun Simulator Tests, measure the performance of a PV module under standard testing procedure to ensure the conforming operability of each PV module); (ii) The thermal performance is measured by following the same approach adopted for solar thermal panels, i.e. stationary conditions, solar simulator with irradiance above $600\,W/m^2$, controlled ambient temperature and no electricity production. When conventional PV and thermal modules are in operation, the actual performance can be calculated from datasheet using ambient temperature, solar irradiance and fluid temperature as input. In particular, the actual PV module temperature is calculated using Nominal Operating Cell Temperature approach and the efficiency correction is determined through the coefficient γ. However, the simultaneous generation of electricity and heat under realistic environmental conditions requires dedicated experimental campaign to assess the mutual interaction between heat and electricity generation. Therefore, an experimental analysis aimed at determining the thermal efficiency was performed at the laboratory SolarTech^{LAB} (Politecnico di Milano, of latitude 45° 30' 10.588" N and longitude 9° 9' 23.677" E), according to the procedure and with the setup discussed earlier [60]. Four PVT modules from Solink [48], with an area of $1.63\,m^2$ and a peak electricity production of $153\,W/m^2$, are considered. The Solink technology adopts roll-bond as heat recovery system applied to conventional PV modules guaranteeing reduced cost as the PV module production is not changed. The contact between the roll bond and the PV module is mechanical (no glue) so as to prevent glue failure over time. The roll-bond is covered with insulating sheet to reduce thermal losses.

The measurements were carried out on five consecutive days, with a sampling time of 1 s, to include a wide range of ambient conditions and fluid temperature. Examples of operation for a typical day are illustrated in Fig. 10. Then, the performance is evaluated on a minute-by-minute base, taking the average of 60 samples, to increase the accuracy and smooth the transients. Finally, the experimental data are filtered to keep only those within a certain operating window of the measuring devices and to eliminate those measured in transient conditions.

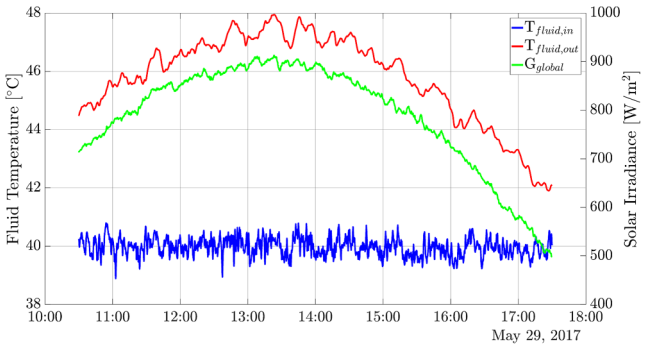

Fig. 10. Temperatures at the inlet and outlet of the PVT modules during a sunny day at the laboratory SolarTech^{LAB} (Politecnico di Milano, latitude 45° 30' 10.588" N, longitude 9° 9' 23.677" E).

The resulting data, as well as the corresponding regression line, are plotted in Fig. 11, which shows the PVT thermal efficiency as function of the reduced temperature $(T_{avg} - T_{amb})/I$, where the color code represents the difference between average fluid and ambient temperature. The linear regression ($R^2 = 0.83$) identifies the parameters introduced in Section 2.2: the optical efficiency $\eta_o = 0.50$ and the empirical coefficient $\alpha = 11.2\,W/(m^2K)$.

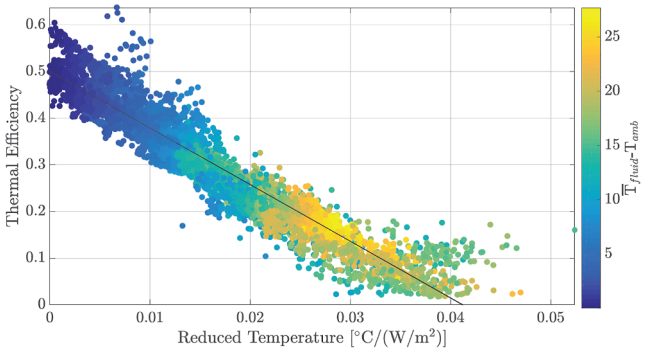

Fig. 11. Thermal efficiency of the PVT modules as function of the reduced temperature and corresponding linear regression. The color code represents the difference between the average fluid and the ambient temperature.

Contrary to the analysis carried out in [60], such parameters allow to evaluate the impact of real-time ambient temperature and solar irradiance on the thermal efficiency. It is worth mentioning that, although such values are provided by the manufacturer, a significant difference is observed by carrying out the experiments under realistic operating conditions (i.e. manufacturer data: $\eta_o = 0.58$ and $\alpha = 15.5$).

Appendix C. Reference ambient conditions

The profiles of ambient temperature and solar irradiance implemented in this work are shown in Fig. 12, on the left- and right-hand side, respectively. Such profiles are those presented in Fig. 3 of reference [43] for Abu Dhabi; a typical day with hour resolution is considered for each month of the year.

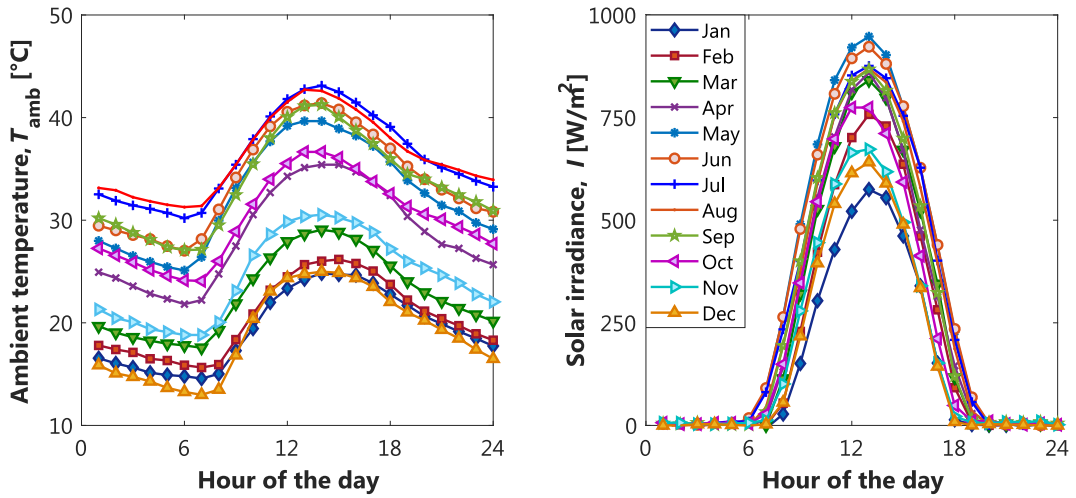

Fig. 12. Hourly profiles of ambient temperature (left) and solar irradiance (right) for an average day in each month the year in Abu Dhabi. Figure adapted from [43].

Appendix D. Impact of humidifier height on cost of clean water

The effects of yearly water production and of humidifier height on the cost of clean water are illustrated in Fig. 13, which shows the cost of potable water as function of the yearly water production (proportional to the installed solar area) for three different humidifier heights and for a fixed electricity price. The cost of potable water decreases with W. This depends on the fact that the produced water increases faster than the capital cost due to the fixed costs and to the nonlinear contribution of the cost of the humidifier. Furthermore, one can note that a taller humidifier translates into higher costs for small system sizes ($W \leqslant W_5^*$), where the higher costs of the humidifier is predominant over the increased performance, and lower costs for bigger sizes ($W \geqslant W_{6.4}^*$), where the increase in system performance is the dominant factor. Here, W_5^* and $W_{6.4}^*$ indicate the values of yearly water production above which $H = 5$ m and 6.4 m are the most convenient solution for the considered electricity price and ambient conditions.

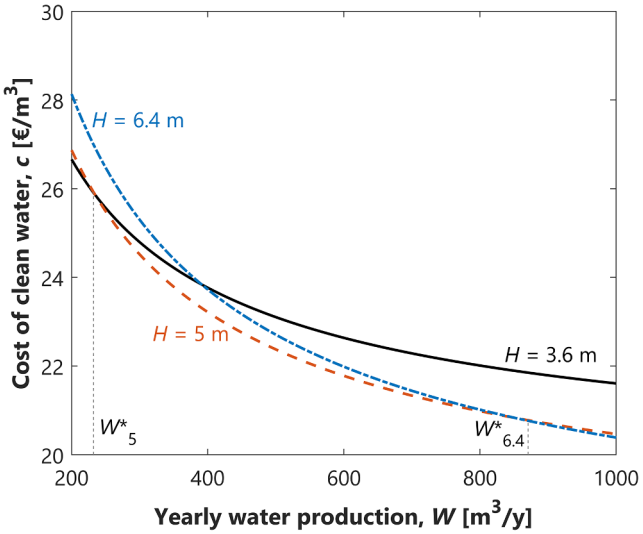

Fig. 13. Cost of clean water as function of yearly water produced for three different heights of the humidifier, namely $H = 3.6$ m (black solid line), 5 m (red dashed line), and 6.4 m (green dotted-dashed line). Fixed cost of electricity, $p = 0.1$ €/kWh, $N_s = 2$.

Appendix E. Supplementary data

Supplementary data associated with this article can be found, in the online version, athttps://doi.org/10.1016/j.ecmx.2019.100004.

References

[1] FAO. Food wastage footprint. Impacts on natural resources. Summary Report. Technical report. Food and Agricolture Organization of the United Nations; 2013.
[2] IRENA. Renewable energy in the water, energy and food nexus, Technical Report January. International Renewable Energy Agency 2015.
[3] International Water Summit. Energy efficient desalination. International Water Summit; 2018. Technical Report January.
[4] Abusharkh AG, Giwa Adewale, Hasan Shadi Wajih. Wind and geothermal energy in desalination: a short review on progress and sustainable commercial processes. Ind Eng Manage 2015;04(04):175.
[5] Abdelkareem Mohammad Ali, Assad Mamdouh El Haj, Sayed Enas Taha, Soudan Bassel. Recent progress in the use of renewable energy sources to power water desalination plants. Desalination 2018;435(September):97–113.
[6] Urban Jeffrey J. Emerging scientific and engineering opportunities within the water-energy nexus. Joule 2017;1(4):665–88.
[7] Zamen Mohammad, Amidpour Majid, Soufari Seyyed Mehdi. Cost optimization of a solar humidification-dehumidification desalination unit using mathematical programming. Desalination 2009;239(1–3):92–9.
[8] Giwa Adewale, Akther Nawshad, Housani Amna Al, Haris Sabeera, Hasan Shadi Wajih. Recent advances in humidification dehumidification (HDH) desalination processes: improved designs and productivity. Renew Sustain Energy Rev 2016;57:929–44.
[9] Karim Bourouni M, Chaibi Thameur, Tadrist Lounes. Water desalination by humidification and dehumidification of air: state of the art. Desalination 2001;137(1–3):167–76.
[10] Müller-Holst Hendrik, Engelhardt Martin, Herve Martinez, Schölkopf Wolfgang. Solarthermal seawater desalination systems for decentralised use. Renewable Energy 1998;14(1–4):311–8.
[11] Prakash Narayan G, Sharqawy Mostafa H, Summers Edward K, Lienhard John H, Zubair Syed M, Antar Mohamed A. The potential of solar-driven humidification-dehumidification desalination for small-scale decentralized water production. Renew Sustain Energy Rev 2010;14(4):1187–201.
[12] Elmutasim Samih M, Ahmed MA, Antar Mohamed A, Gandhidasan P, Zubair Syed M. Design strategies of conventional and modified closed-air open-water humidification dehumidification systems. Desalination 2018;435(October):114–27.
[13] Abu Arabi Mousa K, Reddy Kandi Verlkat. Performance evaluation of desalination processes based on the humidification/dehumidification cycle with different carrier gases. Desalination 2003;156(1–3):281–93.
[14] Prakash Narayan G, McGovern Ronan H, Lienhard John H, Zubair Syed M. Helium as a carrier gas in humidification dehumidification desalination systems. In: Volume 1: Advances in Aerospace Technology; Energy Water Nexus; Globalization of Engineering; Posters, ASME; 2011. pp. 437–444.
[15] Hendrik Müller-Holst. Solar thermal desalination using the multiple effect humidification (MEH)-method. In: Rizzuti Lucio, Mill Ettouney Hisham, Cipollina Andrea, editors. Solar Desalination for the 21st Century: A Review of Modern Technologies and Researches on Desalination Coupled to Renewable Energies. Netherlands, Dordrecht: Springer; 2007. p. 215–25.
[16] Prakash Narayan G, Mistry Karan H, Sharqawy Mostafa H, Zubair Syed M, Lienhard John H. Energy effectiveness of simultaneous heat and mass exchange devices. Front Heat Mass Transfer 2010;1(2).
[17] Prakash Narayan G, Lienhard V John H, Zubair Syed M. Entropy generation minimization of combined heat and mass transfer devices. Int J Therm Sci 2010;49(10):2057–66.
[18] Prakash Narayan G, Chehayeb Karim M, McGovern Ronan K, Thiel Gregory P, Zubair Syed M, John H, Lienhard V. Thermodynamic balancing of the humidification dehumidification desalination system by mass extraction and injection. Int J Heat Mass Transf 2013;57(2):756–70.
[19] Paolo Gabrielli, Marco Mazzotti. Equilibrium theory solution of a solar-driven humidification-dehumidification process for water desalination; 2019.
[20] Mistry Karan H, Mitsos Alexander, John H, Lienhard V. Optimal operating conditions and configurations for humidification- dehumidification desalination cycles. Int J Therm Sci 2011;50(5):779–89.
[21] Zamen Mohammad, Soufari Seyyed Mehdi, Amidpour Majid. Improvement of solar humidification-dehumidification desalination using multi-stage process. Italian Association of Chemical Engineering – AIDIC 2011. vol. 25.
[22] Narayan Prakash G, Maximus G St, John Zubair Syed M, Lienhard V. John H. Thermal design of the humidification dehumidification desalination system: an experimental investigation. Int J Heat Mass Transf 2013;58(1–2):740–8.
[23] Thiel Gregory P, Miller Jacob A, Zubair Syed M, Lienhard John H. Effect of mass extractions and injections on the performance of a fixed-size humidification-dehumidification desalination system. Desalination 2013;314:50–8.
[24] McGovern Ronan K, Thiel Gregory P, Prakash Narayan G, Zubair Syed M, John H, Lienhard V. Performance limits of zero and single extraction humidification-dehumidification desalination systems. Appl Energy 2013;102:1081–90.
[25] Miller Jacob A, John H, Lienhard V. Impact of extraction on a humidification-dehumidification desalination system. Desalination 2013;313:87–96.
[26] Chehayeb Karim M, Prakash Narayan G, Zubair Syed M, John H, Lienhard V. Use of multiple extractions and injections to thermodynamically balance the humidification dehumidification desalination system. Int J Heat Mass Transf 2014;68:422–34.
[27] Chehayeb Karim M, Prakash Narayan G, Zubair Syed M, John H, Lienhard V. Thermodynamic balancing of a fixed-size two-stage humidification dehumidification desalination system. Desalination 2015;369:125–39.
[28] Huang Xin, Li Yang, Ke Tingfen, Ling Xiang, Liu Weihong. Thermal investigation and performance analysis of a novel evaporation system based on a humidification-dehumidification process. Energy Convers. Manage. 2017;147:108–19.
[29] Siddiqui Osman K, Sharqawy Mostafa H, Antar Mohamed A, Zubair Syed M. Performance evaluation of variable pressure humidification-dehumidification systems. Desalination 2017;409:171–82.
[30] Ifras Zubair M, Al-Sulaiman FahadA, Antar Mohammed A, Al-Dini Salem A, Ibrahim Nasiru I. Performance and cost assessment of solar driven humidification dehumidification desalination system. Energy Convers Manage 2017;132:28–39.
[31] Lawal Dahiru U, Zubair Syed M, Antar Mohammad A. Exergo-economic analysis of humidification-dehumidification (HDH) desalination systems driven by heat pump (HP). Desalination 2018;443(March):11–25.
[32] Li Yang, Huang Xin, Peng Hao, Ling Xiang, ShanDong Tu. Simulation and optimization of humidification-dehumidification evaporation system. Energy 2018;145:128–40.
[33] Mahdizade Efaf Z, Ameri Mehran. Thermodynamic investigation of a semi-open air, humidification dehumidification desalination system using air and water heaters. Desalination 2018;428(October 2017):182–98.
[34] He Weifeng, Yang Hongxing, Wen Tao, Han Dong. Thermodynamic and economic investigation of a humidification dehumidification desalination system driven by low grade waste heat. Energy Convers Manage 2018:1–11.
[35] Ismail Mohamed AM, El-Minshawy Nabil. Theoretical investigation of solar humidification-dehumidification desalination system using parabolic trough concentrators. Energy Convers Manage 2011;52(10):3112–9.
[36] Al-Sulaiman FahadA, Ifras Zubair M, Atif Maimoon, Gandhidasan Palanichamy, Al-Dini Salem A, Antar Mohamed A. Humidification dehumidification desalination system using parabolic trough solar air collector. Appl Therm Eng 2015;75:809–16.
[37] Houcine Imed, BenAmara Mahmoud, Guizani Amanallah, Maâlej Mohammed. Pilot plant testing of a new solar desalination process by a multiple-effect-humidification technique. Desalination 2006;196(1–3):105–24.
[38] Yuan Guofeng, Zhang Hefei. Mathematical modeling of a closed circulation solar desalination unit with humidification-dehumidification. Desalination 2007;205(1–3):156–62.
[39] Yuan Guofeng, Wang Zhifeng, Li Hongyong, Li Xing. Experimental study of a solar desalination system based on humidification-dehumidification process. Desalination 2011;277(1–3):92–8.
[40] Ghazal Maher T, Atikol Ugur, Egelioglu Fuat. An experimental study of a solar humidifier for HDD systems. Energy Convers Manage 2014;82:250–8.
[41] Elminshawy Nabil A S, Siddiqui Farooq R, Addas Mohammad F. Experimental and analytical study on productivity augmentation of a novel solar humidification-dehumidification (HDH) system. Desalination 2015;365:36–45.
[42] Wang Jun-hong, Gao Nai-yun, Deng Yang, Li Yong-li. Solar power-driven humidi fi cation – dehumidi fi cation (HDH) process for desalination of brackish water. Des 2012;305:17–23.
[43] Giwa Adewale, Fath Hassan, Hasan Shadi W. Humidification-dehumidification desalination process driven by photovoltaic thermal energy recovery (PV-HDH) for small-scale sustainable water and power production. Desalination 2016;377:163–71.
[44] Elsafi Amin M. Integration of humidification-dehumidification desalination and concentrated photovoltaic-thermal collectors: energy and exergy-costing analysis. Desalination 2017;424(June):17–26.
[45] Flexiring. Koch-Glitsch:http://www.koch-glitsch.com/Document%20Library/KGPP1.pdf; 2018.
[46] Green Don W, Perry Robert H. Perry's chemical engineers' handbook. 8th ed. McGraw-Hill; 2008.
[47] Lienhard IV JH, Lienhard V JH. A heat transfer textbook. 4th ed. Cambridge, MA: Phlogiston Press; 2018. Version 2.12.
[48] Solink.http://www.solink.it/listino/.
[49] Riello.http://www.riello.it/catalogo/domestico/solare-termico; 2018.
[50] AspenPlus V8.6; 2014.
[51] Antonio Rocha J, Bravo Jose L, Fair James R. Distillation columns containing structured packings: a comprehensive model for their performance. 1. Hydraulic models. Ind Eng Chem Res 1993;32(4):641–51.
[52] Brodkey Rober S, Hershey Harry C. Transport phenomena: a unified approach. New York: McGraw-Hill Chemical Engineering Series; 2003.
[53] Zhang Ying, Chen Hern, Chen Chau-chyun, Plaza Jorge M, Dugas Ross, Rochelle Gary T. Rate-Based Process Modeling study of CO_2 capture with aqueous monoethanolamine solution. Ind. Eng. Chem. Res. 2009;48(20):9233–46.
[54] Plaza Jorge M, Van Wagener David, Rochelle Gary T. Modeling CO2 capture with aqueous monoethanolamine. Int J Greenhouse Gas Control 2010;4(2):161–6.
[55] Jilvero Henrik, Normann Fredrik, Andersson Klas, Johnsson Filip. Thermal integration and modelling of the chilled ammonia process. Energy Procedia 2011;4:1713–20.
[56] Hai Yu, Qi Guojie, Wang Shujuan, Morgan Scott, Allport Andrew, Cottrell Aaron, Do Thong, McGregor James, Wardhaugh Leigh, Feron Paul. Results from trialling aqueous ammonia-based post-combustion capture in a pilot plant at Munmorah Power Station: Gas purity and solid precipitation in the stripper. Int J Greenhouse Gas Control 2012;10:15–25.

[57] Jingwen Yu, Wang Shujuan, Hai Yu, Wardhaugh Leigh, Feron Paul. Rate-based modelling of CO_2 regeneration in ammonia based CO_2 capture process. Int J Greenhouse Gas Control 2014;28:203–15.
[58] Li Kangkang, Hai Yu, Tade Moses, Feron Paul. Theoretical and experimental study of NH3 suppression by addition of Me(II) ions (Ni, Cu and Zn) in an ammonia-based CO2 capture process. Int J Greenhouse Gas Control 2014;24(X):54–63.
[59] Pérez-Calvo Jose Francisco, Sutter Daniel, Gazzani Matteo, Mazzotti Mazzotti. Pilot tests and rate-based modelling of CO2 capture in cement plants using an aqueous ammonia solution. Chem Eng Trans 2018;69(i):145–50.
[60] Bombarda Paola, Di Marcoberardino Gioele, Lucchini Andrea, Leva Sonia, Manzolini Giampaolo, Molinaroli Luca, Pedranzini Federico, Simonetti Riccardo. Thermal and electric performances of roll-bond flat plate applied to conventional PV modules for heat recovery. Appl Therm Eng 2016;105:304–13.
[61] Moradi Kamran, Ali Ebadian M, Lin Cheng Xian. A review of PV/T technologies: effects of control parameters. Int J Heat Mass Transf 2013;64:483–500.
[62] Dupeyrat Patrick, Ménézo Christophe, Wirth Harry, Rommel Matthias. Improvement of PV module optical properties for PV-thermal hybrid collector application. Sol Energy Mater Sol Cells 2011;95(8):2028–36.
[63] Aste Niccolò, Leonforte Fabrizio, Del Pero Claudio. Design, modeling and performance monitoring of a photovoltaic-thermal (PVT) water collector. Sol Energy 2015;112:85–99.
[64] Chow Tin Tai. A review on photovoltaic/thermal hybrid solar technology. Appl Energy 2010;87(2):365–79.
[65] Allan James, Dehouche Zahir, Stankovic Sinisa, Mauricette Lascelle. Performance testing of thermal and photovoltaic thermal solar collectors. Energy Sci Eng 2015;3(4):310–26.
[66] Simonetti Riccardo, Molinaroli Luca, Manzolini Giampaolo. Development and validation of a comprehensive dynamic mathematical model for hybrid PV/T solar collectors. Appl Therm Eng 2018;133(January):543–54.
[67] Shahzad Muhammad Wakil, Burhan Muhammad, Ang Li, Ng Kim Choon. Energy-water-environment nexus underpinning future desalination sustainability. Desalination 2017;413:52–64.
[68] Copeland Thomas E, Weston Fred J. Financial theory and corporate policy. 3rd ed. Addison-Wesley Publishing Company Inc; 1988.
[69] Brunazzi Enrico, Nardini Giorgio, Pagliani Andrea. An economical criterion for packed absorption column design. Chem Biochem Eng Q 2002;16(4):199–206.
[70] Raghu MR, Karthik Ramesh NC, Dheenathayalan Rajesh, Naheem Irfan Ahmed. GCC WACC – H1 2017 A toolkit for Corporate Financiers. Marmore; 2017. p. 2017. Technical report.
[71] Abu Dhabi Distribution Co. Water & Electricity Tariffs 2017. Technical report, Abu Dhabi Distribution Co., Abu Dhabi; 2017.
[72] Vartiainen Aero, Masson Gaetan, Breyer Christian. The true competitiveness of solar PV.A European case study. Technical report. Eur Technol Innovation Platform 2017.
[73] Gabrielli Paolo, Gazzani Matteo, Martelli Emanuele, Mazzotti Marco. Optimal design of multi-energy systems with seasonal storage. Appl Energy 2018;219:408–24.
[74] Personal communications with industry experts; 2018.
[75] Ramos Alba, Guarracino Ilaria, Mellor Alexander, Alonso-álvarez Diego, Childs Peter, Ekins-daukes Nicholas J, Markides Christos N. Solar-thermal and hybrid photovoltaic-thermal systems for renewable heating. Technical Report 22. Imperial College London 2017.
[76] African Development Bank Group. Renewable Energy in Africa – Tanzania Country Profile. Technical report; 2015.